

Thermal infrared emissivity measurements under a simulated lunar environment: Application to the Diviner Lunar Radiometer Experiment

Kerri L. Donaldson Hanna,¹ Michael B. Wyatt,¹ Ian R. Thomas,² Neil E. Bowles,² Benjamin T. Greenhagen,³ Alessandro Maturilli,⁴ Joern Helbert,⁴ and David A. Paige⁵

Received 12 May 2011; revised 18 November 2011; accepted 19 November 2011; published 31 January 2012.

[1] We present new laboratory thermal infrared emissivity spectra of the major silicate minerals identified on the Moon measured under lunar environmental conditions and evaluate their application to lunar remote sensing data sets. Thermal infrared spectral changes between ambient and lunar environmental conditions are characterized for the first time over the $400\text{--}1700\text{ cm}^{-1}$ ($6\text{--}25\text{ }\mu\text{m}$) spectral range for a fine-particulate mineral suite including plagioclase (albite and anorthite), pyroxene (enstatite and augite), and olivine (forsterite). The lunar environment introduces observable effects in thermal infrared emissivity spectra of fine particulate minerals, which include: (1) a shift in the Christiansen feature (CF) position to higher wave numbers (shorter wavelengths), (2) an increase in the overall spectral contrast, and (3) decreases in the spectral contrast of the reststrahlen bands and transparency features. Our new measurements demonstrate the high sensitivity of thermal infrared emissivity spectra to environmental conditions under which they are measured and provide important constraints for interpreting new thermal infrared data sets of the Moon, including the Diviner Lunar Radiometer Experiment onboard NASA's Lunar Reconnaissance Orbiter. Full resolution laboratory mineral spectra convolved to Diviner's three spectral channels show that spectral shape, CF position and band ratios can be used to distinguish between individual mineral groups and lunar lithologies. The integration of the thermal infrared CF position with near infrared spectral parameters allows for robust mineralogical identifications and provides a framework for future integrations of data sets across two different wavelength regimes.

Citation: Donaldson Hanna, K. L., M. B. Wyatt, I. R. Thomas, N. E. Bowles, B. T. Greenhagen, A. Maturilli, J. Helbert, and D. A. Paige (2012), Thermal infrared emissivity measurements under a simulated lunar environment: Application to the Diviner Lunar Radiometer Experiment, *J. Geophys. Res.*, 117, E00H05, doi:10.1029/2011JE003862.

1. Introduction

[2] Our current understanding of lunar surface mineralogy largely comes from laboratory analyses of returned Apollo samples [e.g., Taylor *et al.*, 2001, 2003; Isaacson *et al.*, 2011], lunar meteorites [e.g., Jolliff *et al.*, 2006; Isaacson *et al.*, 2009, 2010], and remote near infrared spectroscopic measurements from Earth-based telescopes [e.g., McCord *et al.*, 1981; Pieters, 1993] and lunar orbiters like Clementine,

Chandrayaan-1's Moon Mineralogy Mapper (M³), and the SELENE Multiband Imager (MI) and Spectral Profiler (SP) [e.g., Tompkins and Pieters, 1999; Matsunaga *et al.*, 2008; Ohtake *et al.*, 2009; Pieters *et al.*, 2009]. Apollo samples provide detailed compositional analysis of a limited number of sites concentrated on the lunar nearside while lunar meteorites are from unknown locations. Soil and rock samples collected at each of the Apollo landing sites have also been well characterized by the Lunar Soil Characterization Consortium (LSCC) [Taylor *et al.*, 2001, 2003] and the Lunar Rock and Mineral Characterization Consortium [Isaacson *et al.*, 2011]. Detailed laboratory analyses of soils, whole rocks, and separates of major mineral phases have determined modal mineralogy, mineral and glass chemistry, agglutinate abundance, and degree of space weathering for each sample at different particle size fractions. These detailed analyses, including laboratory visible (V) to near infrared (NIR) spectroscopic measurements of lunar soils, rocks, meteorites, and mineral separates [Taylor *et al.*, 2001, 2003; Isaacson *et al.*, 2009, 2010, 2011], have provided calibration standards for remote VNIR measurements.

¹Department of Geological Sciences, Brown University, Providence, Rhode Island, USA.

²Atmospheric, Oceanic and Planetary Physics, Clarendon Laboratory, University of Oxford, Oxford, UK.

³Geophysics and Planetary Geosciences Group, Jet Propulsion Laboratory, Pasadena, California, USA.

⁴Experimental Planetary Physics, Institute of Planetary Research, German Aerospace Center, Berlin, Germany.

⁵Department of Earth and Space Sciences, University of California, Los Angeles, Los Angeles, California, USA.

Table 1. Comparison of a Selection of Orbital Thermal Infrared Instruments Used for Earth, Moon, and Mars Remote Sensing^a

Instrument	Planetary Body	Wavelength Range	Spectral Sampling	Number of Channels	Pixel Size	Spatial Coverage
TES	Mars	6–50 μm (1650–200 cm^{-1})	10 cm^{-1} 5 cm^{-1}	143 286	3 × 6 km	global
THEMIS	Mars	0.425–0.86 μm 6.78–14.88 μm	0.1 μm 1 μm	5 9	19 m 100 m	17% global
MCS	Mars	0.3–3.0 μm 11.5–12.2 μm 15.0–16.8 μm 20.0–25.0 μm 29.4–45.4 μm	2.7 μm 0.7 μm 0.7 μm 5.0 μm 4.9 μm	1 1 3 1 3	105 km^2 105 km^2 105 km^2 105 km^2 105 km^2	<20% <20% <20% <20% <20%
ASTER	Earth	0.52–0.86 μm 1.6–2.43 μm 8.125–11.65 μm	0.1 μm 1.2 μm 0.35, 0.7 μm	3 6 5	15 m 30 m 90 m	global global global
DIVINER	Moon	0.35–2.8 μm 7.55–8.68 μm 13–400 μm	2.45 μm 0.5, 0.5, 0.3 μm 10, 16, 50, 300 μm	2 3 4	<500 m <500 m <500 m	50%+ 50%+ 50%+

^aYamaguchi et al. [1998], Christensen et al. [2001, 2004], McCleese et al. [2007], and Paige et al. [2010a].

[3] Earth-based VNIR telescopic observations of the Moon [e.g., McCord et al., 1981; Pieters, 1993] have focused on the central peaks of complex craters on the lunar nearside where materials from greater depths are excavated and where larger exposures of fresh materials are easier to analyze for mineralogical absorptions. Recently, high spatial and spectral resolution VNIR observations from the SELENE SP (296 channels from 0.5–2.6 μm with a footprint of 500 m) and MI (9 channels from 0.415–1.55 μm with a footprint of 20 m at visible wavelengths and 62 m at near infrared wavelengths) and M³ (85 channels from 0.46–3.0 μm at 140 m/pixel) have uniquely identified iron-bearing crystalline plagioclase in central peaks, floors, walls and ejecta of several large highland craters [Matsunaga et al., 2008; Ohtake et al., 2009] and the Inner Rook Mountains in the Orientale Basin [Pieters et al., 2009]. SP and M³ observations also confirmed identifications of olivine bearing units in the Copernicus and Aristarchus craters [Mustard et al., 2010; Yamamoto et al., 2010] as well as mapping olivine-bearing units in concentric rings around the South Pole-Aitken, Imbrium, and Moscoviense impact basins [Yamamoto et al., 2010].

[4] Remote sensing at thermal infrared (TIR) wavelengths is of particular interest because silicate minerals (which dominate the surface of most rocky planetary bodies) display fundamental molecular vibration bands due to Si-O stretching and bending vibrations over the ~ 400 –1700 cm^{-1} (6–25 μm) spectral range. These vibrational bands, also known as reststrahlen bands (RB), have long been identified as diagnostic of composition [e.g., Lyon, 1964]. While some previous Earth-based TIR telescopic observations have been made of the Moon [e.g., Hunt and Salisbury, 1969; Murcray et al., 1970; Sprague et al., 1992], previously no multiband TIR camera or spectrometer has been put into orbit to collect measurements. The Diviner Lunar Radiometer Experiment (DLRE) onboard the Lunar Reconnaissance Orbiter (LRO) is the first TIR instrument to provide global coverage maps of TIR derived compositions and physical properties [Glotch et al., 2010; Greenhagen et al., 2010; Paige et al., 2010a, 2010b; Bandfield et al., 2011].

[5] Diviner follows a long line of successful TIR radiometers and spectrometers for Earth and Mars (Table 1) including the Mars Climate Sounder (MCS) on the Mars Reconnaissance Orbiter (MRO). Diviner is a pushbroom

mapper that has nine channels: two broadband solar reflectance channels, three narrowband channels near 8 μm , and four broad thermal channels and a field of view of approximately 200 m [Paige et al., 2010a]. Diviner is nearly identical to MCS with the exceptions of channel band passes, which have been optimized for making lunar thermal infrared measurements, and thermal design. The three 8 μm region channels of Diviner (centered at 7.81, 8.28, and 8.55 μm) were chosen specifically to determine the wavelength position of the Christiansen feature (CF) [Greenhagen, 2009; Greenhagen et al., 2010].

[6] In this paper we characterize the TIR spectral changes between ambient and lunar environment conditions over the 400–1700 cm^{-1} (6–25 μm) spectral range for a fine-particulate mineral suite and evaluate their application to lunar remote sensing data sets. We create a new spectral database of pure minerals of known compositions measured under simulated lunar environmental conditions. Although most of the lunar regolith is composed of a complex mixture of minerals, glasses and agglutinates, we begin with minerals to follow the heritage of other spectral databases [Christensen et al., 2000; Pieters and Hiroi, 2004; Clark et al., 2007; Maturilli et al., 2008] to understand how the spectral features of pure minerals change as the environment under which they are measured change. We address the effects of a simulated lunar environment (SLE) on spectra for each of the major mineral groups observed on the Moon (plagioclase, pyroxene, and olivine). Starting with 2 cm^{-1} resolution laboratory emissivity spectra we observe that under SLE conditions: (1) the CF position shifts to higher wave numbers (shorter wavelengths), (2) the overall spectral contrast increases, and (3) the spectral contrast of the RB and transparency features (TF) decreases. Next we use re-sampled laboratory spectra to determine what constraints can be placed on the lunar surface composition using the limited number of Diviner spectral bands. We discuss three ways in which to distinguish between mineral groups: (1) the general spectral shape of mineral spectra, (2) the CF position, and (3) band ratios. With a limited number of spectral bands, the general shape of mineral spectra can be identified by being concave up or down. The CF position is calculated using a second-order polynomial fit to the re-sampled mineral spectra and analyzed to determine this technique's accuracy. Two spectral band ratios that characterize general

trends of the concavity and the slope of the spectra are analyzed to distinguish between mineral groups, a mineral mixture and lunar soils. Last, we demonstrate the utility of integrating TIR spectral band ratios with well-characterized VNIR spectral parameters of the Clementine and M³ when applied to mixtures specifically. This study thus demonstrates the effectiveness of applying laboratory TIR spectra to constrain lunar surface compositions as well as the importance of integrating data sets across multiple wavelength regions.

2. Background

[7] TIR spectra of planetary surfaces have diagnostic features indicative of rock and mineral compositions. These include: (1) the CF, an emissivity maximum resulting from a rapid change in the refractive index just short ward of the fundamental molecular vibration bands, (2) the RB, the fundamental molecular vibration bands due to Si-O stretching and bending motions, and (3) TF, emissivity minima caused by volume scattering in a spectral region of relative transparency between the principal RB. *Conel* [1969] found that the CF position in silicates is diagnostic of mineralogy and average composition and changes with the change in bond strength and molecular geometry associated with changing mineralogy. *Logan et al.* [1973] and *Salisbury and Walter* [1989] characterized the CF position shift to shorter wavelengths (higher wave numbers) when particulate rock samples are measured under vacuum conditions. *Logan and Hunt* [1970] also observed that emission spectra of particulate silicates under simulated lunar conditions show that the spectral contrast of the CF maximum is greatly enhanced while the spectral contrast of the RB decrease. Of the known silicate minerals on the Moon, plagioclase feldspars, which have little Fe and higher Al and Ca, have shorter wavelength positions for the CF than pyroxenes and olivines which have high Fe and/or Mg and no Al. The RB absorption positions, shapes and intensities, and number of absorptions are dependent on masses, geometry between atoms, and bond strengths between anions and cations within a crystal lattice. Thus, each mineral has a diagnostic set of RB absorptions owing to each mineral's unique composition and/or crystal structure [e.g., *Lyon*, 1964; *Conel*, 1969; *Salisbury and Walter*, 1989; *Hamilton*, 2000]. TF, like the CF, are indicators of mineral compositions and there is a higher-probability of determining specific rock type compositions if both the CF and TF are used for interpretations [*Salisbury and Walter*, 1989; *Cooper et al.*, 2002]. As particles decrease in size, the spectral contrast of the TF increases.

[8] On the Moon small particle size fractions and vacuum-induced thermal gradients complicate the analysis of lunar TIR spectra. Reflectance and emissivity measurements of bulk lunar soils are dominated by the finest particle size fraction (<45 μm) [*Pieters et al.*, 1993]. This is partly due to fine particles coating larger particles and that photons entering a larger particle are unlikely to escape. Furthermore, *Fischer* [1995] showed that optically, the 10–20 μm and 20–45 μm size fractions are most similar to the bulk soil. It has been shown for fine-particulate materials that a vacuum environment can introduce thermal gradients that will alter the spectral emissivity of a surface [*Logan et al.*, 1973]. As

pressure decreases, the spectral contrast increases, and the increased absorption in the RB spectral region (~ 833 – 1250 cm^{-1} ; 8–12 μm) can cause the CF to shift to shorter wavelengths. Other possible causes for the CF to shift to shorter wavelengths include: an increase in blackbody radiance at shorter wavelengths caused by the large subsurface temperature gradient and/or the most transparent portion of a spectrum is at wavelengths shorter than the CF measured under ambient conditions; therefore radiation from deeper, hotter layers of the subsurface are observed [*Hapke*, 1996]. The shift of the CF and how Diviner measures it is significant for the accurate identification and classification of lunar lithologies. Although the lunar surface is a complicated surface for remote sensing analysis, early TIR telescopic observations [*Hunt and Salisbury*, 1964; *Murcray*, 1965; *Goetz*, 1968; *Murcray et al.*, 1970; *Sprague et al.*, 1992] demonstrated that not only did the thermal emission from the Moon differ from blackbody radiation, but that spectral differences owing to compositional differences of the surface existed between lunar locations.

3. Experimental Setup and Samples

[9] Laboratory emissivity measurements of minerals, rocks, and lunar soils made under lunar-like conditions at TIR wavelengths are necessary for the analysis of TIR data from Diviner. However, a complete database of laboratory emissivity spectra measured from the VNIR to TIR wavelengths of minerals, rocks, and lunar soils of varying compositions and particle sizes has not previously existed. Thus for this study, both laboratory emissivity (TIR) and reflectance (VNIR) spectra of minerals were analyzed as well as reflectance spectra of lunar soils (VNIR and TIR) to build a complete data set across multiple wavelength regions.

3.1. Oxford University Lunar Environment Chamber

[10] A new emission chamber in the Atmospheric, Oceanic, and Planetary Physics Department at the University of Oxford has been built to simulate the temperatures and pressures experienced on the lunar surface [*Thomas et al.*, 2010]. The chamber is attached to the emission port of a Bruker IFS-66v/S Fourier Transform Spectrometer and spectral measurements are made under two conditions: ambient (sample cup is heated to approximately 350–370 K and pressure = 1 bar of nitrogen) and a simulated lunar environment (SLE) (sample cup is heated to approximately 500 K, interior chamber is cooled to 150 K, and pressure < 10^{-3} mbar). A potassium bromide (KBr) emission port window, KBr beamsplitter, and a Deuterated L-alanine doped Triglyceride Sulphate (DLATGS) detector allow laboratory emissivity spectra to be collected at a resolution of 2 cm^{-1} over the 345 – 3030 cm^{-1} (3.3–29 μm) spectral range [*Thomas et al.*, 2010]. In this study, we make new laboratory emissivity measurements of a fine (<25 μm) particulate mineral suite under SLE conditions. The mineral suite includes the major silicate minerals identified or inferred on the lunar surface (plagioclase end-members anorthite and albite; clinopyroxene and orthopyroxene; the olivine end-member forsterite). These mineral samples are well-characterized samples from Arizona State University (ASU) [*Christensen et al.*, 2000] and *Greenhagen* [2009].

Table 2. Mineral Sample Chemistry^a

Mineral	Sample ID	Source	SiO ₂	TiO ₂	Al ₂ O ₃	Cr ₂ O ₃	Fe ₂ O ₃	FeO	MnO	MgO	CaO	Na ₂ O	K ₂ O	P ₂ O ₅
Albite	WAR-0235	ASU	68.3	0.03	19.98	0.02	0	0.33	0.01	0.04	0.01	11.54	0.02	0.03
Anorthite	BUR-340	ASU	43.2	0	35.62	0	0	0.54	0.01	0.39	17.58	0.84	0.01	0
Augite	BUR-620	ASU	50.51	0.11	1.69	0	0	16.2	0.73	7.58	21.51	1.91	0	0
Augite	AugiteB	UCLA	53.04	0.03	0.85	0.07	0	9.85	0.26	11.82	23.58	0.54	0.01	0
Augite	Augite1	BED	56.45	0.221	0.95	0	6.96	4.97	547 ppm	13.70	18.41	1.06	0.08	<0.01
Augite	Augite2	BED	46.20	1.62	7.06	0	7.53	3.99	0.08 ppm	14.67	19.51	0.56	0.18	0.04
Diopside	Diopside	BED	54.3	402 ppm	0.845	3.3 ppm	0	0.40	118 ppm	21.7	18.6	<2.00	832 ppm	<177 ppm
Enstatite	Enstatite	BED	49.00	1.354	7.12	0	6.15	0	184 ppm	26.09	0.63	0.20	2.79	0.144
Enstatite	EnstatiteB	UCLA	53.88	0.10	3.48	0.13	0	13.30	0.25	28.56	0.66	0.12	0.02	0
Fayalite	Fayalite	BED	28.7	0.041	0.31	0	66.50	0	22496 ppm	0.78	0.24	<0.05	0.06	0.127
Forsterite	AZ-01	ASU	40.62	0	0	0	0	8.82	0.12	48.99	0.07	0	0	0
Hypersthene	Hypersthene2	BED	51.68	0.593	6.46	0	10.56	0	1348 ppm	24.59	2.57	1.02	0.16	0.061
Olivine	Olivine1	BED	42.51	0.60	4.73	0	9.28	0	1146 ppm	35.96	3.18	0.26	0.23	0.251

^aRuff [1998], Christensen et al. [2000], Maturilli et al. [2008], and Greenhagen [2009].

Mineral chemistry data for all mineral samples are listed in Table 2.

3.2. Berlin Emissivity Database

[11] Additional full resolution laboratory emissivity spectra made under ambient conditions are included in our study to extend the compositional range of our samples. Thermal emission measurements were made at the Planetary Emissivity Laboratory at Deutschen Zentrum für Luft- und Raumfahrt e.V. (DLR) at a resolution of 4 cm⁻¹ over the 455–1429 cm⁻¹ (7.0–22.0 μm) spectral range using a Fourier transform infrared spectrometer Bruker IFS 88, purged with dry air and equipped with a liquid nitrogen cooled HgCdTe (MCT) detector [Maturilli et al., 2008]. Previously measured fine (<25 μm) particle size fractions of plagioclase (full plagioclase solid solution series from Ca-rich anorthite to Na-rich albite), low- and high-Ca pyroxenes, and olivine are included in our study. A 50/50 wt% mineral mixture of anorthite and olivine as well as its mixture end-members are also examined. Chemistry data for available mineral samples are listed in Table 2.

3.3. RELAB

[12] Brown University's Reflectance Experiment Laboratory (RELAB) has built an extensive spectral library of VNIR as well as TIR reflectance spectral measurements of lunar analog materials as well as lunar soil samples. Spectral measurements were made with a Thermo Nicolet Nexus 870 spectrometer at a resolution of 4 cm⁻¹ over the 400–10000 cm⁻¹ (1.0–25.0 μm) spectral range [Pieters and Hiroi, 2004]. To put our new emissivity measurements into the context of lunar lithologies observed on the surface, previously measured TIR reflectance spectra of Apollo lunar soil samples characterized by the Lunar Soil Characterization Consortium (LSCC) [Taylor et al., 2001, 2003] are also analyzed. In this study, spectral measurements for the lunar soil samples are of the 10–20 μm particle size fraction. Lunar mare soil samples chosen for this study include soils from the Apollo 11, 12, 15 and 17 landing sites (10084, 12001, 12030, 15041, 15071, 71061, 71501, 70181, and 79221) [Taylor et al., 2001] and highlands soil samples from the Apollo 16 landing site (61141, 61221, 62331, 64801, 67471, and 67481) [Taylor et al., 2003]. Compositions based on LSCC determined modal mineralogies of the Apollo lunar soils are plotted on a plagioclase-orthopyroxene-clinopyroxene ternary

diagram in Figure 1 [Stoeffler et al., 1980] and the modal mineralogies are available in Table 3.

4. Results

[13] Results for full resolution (2 cm⁻¹) laboratory emissivity spectra of the mineral groups (plagioclase, pyroxene, and olivine) measured under ambient and simulated lunar environment conditions will first be discussed in terms of general trends observed among all mineral groups and then spectral feature changes within each mineral group will be discussed in detail. Full resolution mineral spectra are then re-sampled to Diviner's three 8 μm region channels and

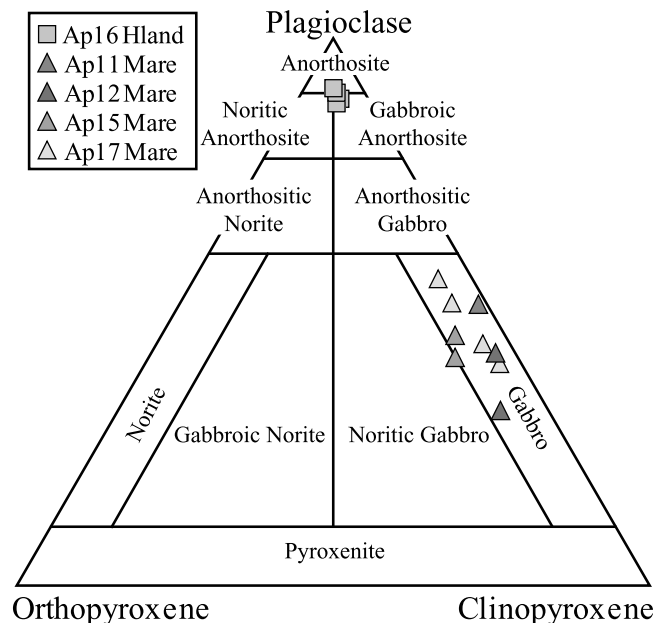


Figure 1. Lunar highland and mare soils collected at the Apollo 11, 12, 15, 16, and 17 landing sites plotted on a Plagioclase-Orthopyroxene-Clinopyroxene ternary diagram based on modal mineralogies determined by the Lunar Soil Characterization Consortium (LSCC) [Taylor et al., 2001, 2003]. Soil samples include: 10084, 12001, 12030, 15041, 15071, 61141, 61221, 62331, 64801, 67471, 67481, 71061, 71501, 70181, and 79221.

Table 3. LSCC Apollo Lunar Soil Modal Mineralogy for the 10–20 μm Particle Size Fraction^a

Apollo Sample	Type	Plag	Opx	Pig	Mg-Cpx	Fe-Cpx	Ilm	Olv	Agg Glass	Vol Glass	Others
10084	Mare	17.1	0.61	3.23	7.81	0.57	5.2	1.1	57.0	2.9	4.5
12001	Mare	13.9	2.24	7.36	7.64	0.70	1.8	4.2	56.8	1.3	3.8
12030	Mare	14.0	2.86	10.18	6.59	1.75	3.2	3.7	49.8	1.5	6.4
15041	Mare	16.2	2.35	8.14	5.12	1.37	0.8	2.4	56.7	2.6	4.3
15071	Mare	19.4	2.13	7.64	5.56	1.38	1.8	2.8	49.2	4.1	6.0
71061	Mare	15.2	1.32	4.07	5.97	1.12	9.7	4.5	37.9	18.8	1.3
71501	Mare	19.8	1.47	4.61	6.34	1.25	9.7	3.4	44.8	7.5	1.1
70181	Mare	18.3	1.20	2.57	3.74	0.97	6.7	3.8	51.7	9.2	1.8
79221	Mare	16.0	1.64	2.86	3.24	1.82	6.0	3.4	54.3	9.2	1.4
61141	Hlands	40.3	1.69	2.15	1.45	0.04	0.3	1.6	53.9	0.0	0.6
61221	Hlands	59.4	1.82	1.43	1.95	0.14	0.3	2.0	32.6	0.0	0.4
62331	Hlands	37.8	1.99	1.55	1.74	0.05	0.5	1.7	55.0	0.0	0.6
64801	Hlands	34.5	1.24	0.96	0.60	0.01	0.2	1.0	61.0	0.0	0.5
67461	Hlands	61.0	1.47	1.07	1.52	0.05	0.3	1.5	32.4	0.0	0.7
67481	Hlands	62.0	2.55	1.27	1.73	0.13	0.2	2.9	28.6	0.0	0.7

^aTaylor et al. [2001, 2003].

published spectral parameters used in Diviner analyses [Glotch et al., 2010; Greenhagen et al., 2010] are calculated and discussed. We finish with a discussion on the integration of well-established NIR spectral parameters (spectral curvature and 1 μm band minimum) with the TIR CF wavelength position measured under a simulated lunar environment.

4.1. Full Resolution Emissivity Spectra: Ambient Versus Simulated Lunar Environment

[14] Full resolution laboratory emissivity spectra for each mineral group (plagioclase, clinopyroxene, orthopyroxene, and olivine) are plotted in Figure 2. In Figure 2, left, are spectra measured under ambient conditions and on the right are spectra measured under a simulated lunar environment

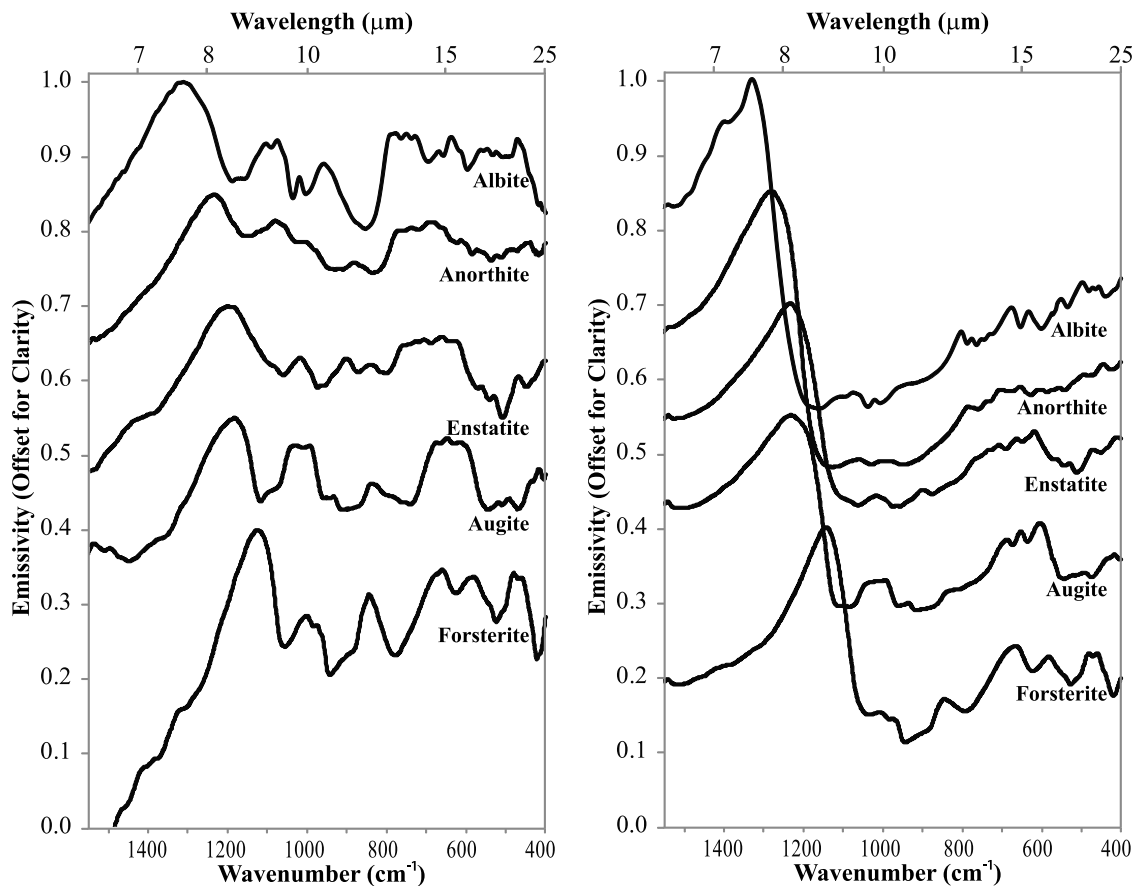


Figure 2. (left) Full resolution laboratory spectra of fine particulate minerals (0–25 μm) measured under ambient conditions. (right) Full resolution laboratory spectra of the same minerals measured under SLE conditions. Spectra are normalized to 1.0 at peak emission and offset by 0.15 emissivity from one another for clarity.

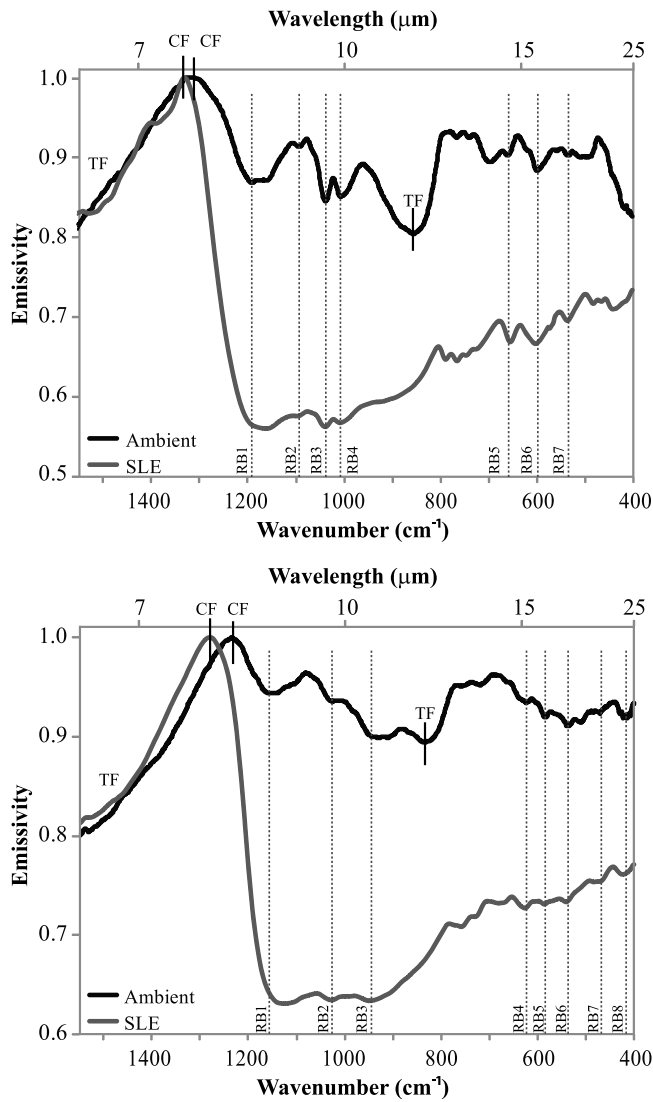


Figure 3. (top) Full resolution laboratory spectra of the fine particulate mineral albite (0–25 μm) measured under ambient and SLE conditions. (bottom) Full resolution laboratory spectra of the fine particulate mineral anorthite (0–25 μm) measured under ambient and SLE conditions. CF and TF positions are indicated by solid vertical lines. RB absorptions identified in ambient spectra are designated by dotted vertical lines.

(SLE). Wavelength positions of the CF, RB absorptions, and TF are indicated for each mineral sample in Figures 3, 4, and 5 and positions are listed in Table 4. CF positions were determined by fitting a second-order polynomial to the 1110–1428 cm⁻¹ region and equating the CF position to the frequency of the emission peak. Several observations can be made regarding mineral separates measured under SLE conditions: (1) the CF position shifts to higher wavenumbers (shorter wavelengths), (2) the overall spectral contrast increases, (3) the spectral contrast of the RB absorptions between ~1100 and 800 cm⁻¹ (9–12 μm) and between 400 and 625 cm⁻¹ (16 and 25 μm) decrease, (4) the spectral contrast of the TF decrease and are not identifiable in albite, anorthite, enstatite, and augite spectra, and (5) the

spectral contrast of the TF at wavelengths short ward of the CF does not change between ambient and SLE conditions, however the spectral contrast from the CF to the principal RB increases dramatically. Further details regarding the observed differences for each mineral group are discussed below.

[15] Focusing just on the differences observed in the CF, our spectral measurements agree with earlier measurements by Logan *et al.* [1973] and Salisbury and Walter [1989] that the CF position shifts to shorter wavelengths under SLE conditions. Salisbury and Walter [1989] found a linear trend between the CF position measured under ambient and SLE conditions with a $R^2 = 0.9773$ as seen in Figure 6. This study

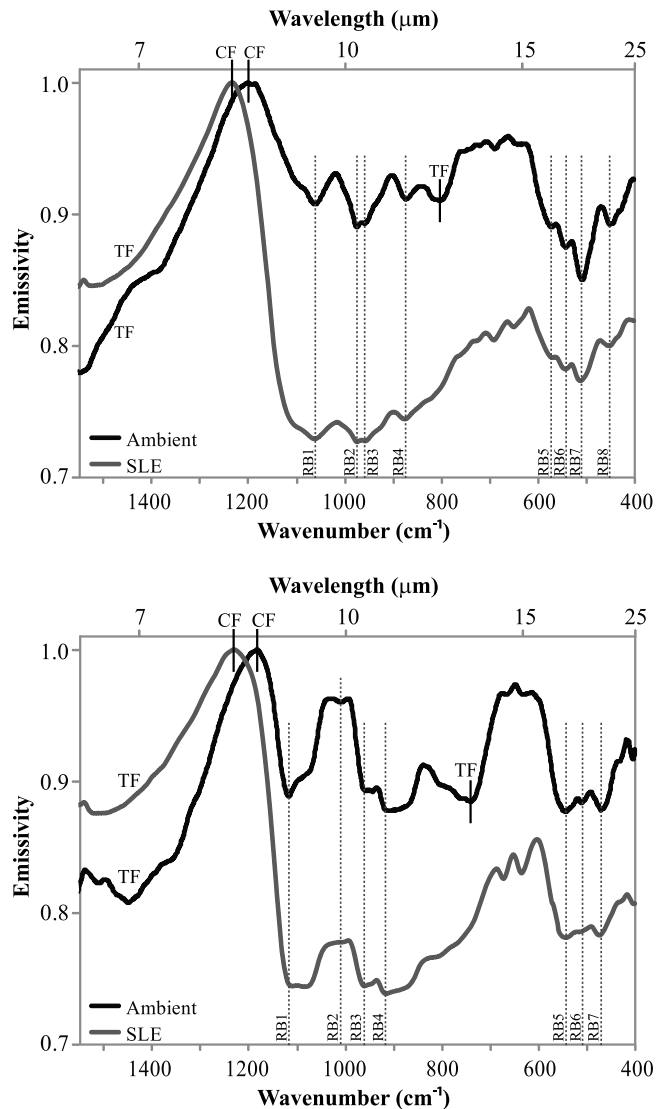


Figure 4. (top) Full resolution laboratory spectra of the fine particulate mineral enstatite (0–25 μm) measured under ambient and SLE conditions. (bottom) Full resolution laboratory spectra of the fine particulate mineral augite (0–25 μm) measured under ambient and SLE conditions. CF and TF positions are indicated by solid vertical lines. RB absorptions identified in ambient spectra are designated by dotted vertical lines.

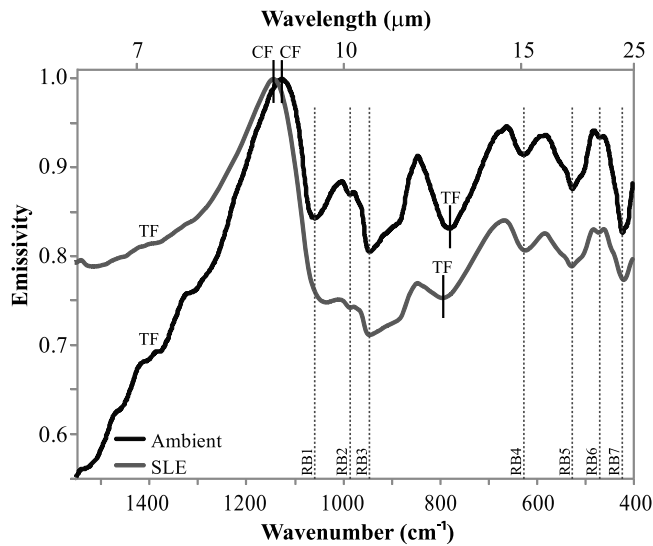


Figure 5. Full resolution laboratory spectra of the fine particulate mineral forsterite (0–25 μm) measured under ambient and SLE conditions. CF and TF positions are indicated by solid vertical lines. RB absorptions identified in the ambient spectrum are designated by dotted vertical lines.

focused on powdered rock samples of varying compositions from felsic to mafic. SLE measurements were made by *Logan et al.* [1973] using one lab setup and the ambient conditions were made by *Salisbury and Walter* [1989] using a second lab setup. A linear trend between the CF position measured under ambient and SLE conditions was also found with our fine particulate mineral spectra (Figure 6). Our linear trend is displaced from the Salisbury and Walter trend, has a higher slope value, and a lower R^2 value ($R^2 = 0.8516$). While the two trends are similar, there are differences which could result from: (1) the powdered rock measurements being made in 2 different lab setups [*Logan et al.*, 1973; *Salisbury and Walter*, 1989], (2) powdered rock samples [*Logan et al.*, 1973; *Salisbury and Walter*, 1989] versus powdered mineral samples (this study), (3) laboratory reflectance [*Salisbury and Walter*, 1989] versus laboratory emissivity data [*Logan et al.* [1973] and this study), and (4) our SLE conditions varying from *Logan et al.*'s [1973] heating from above SLE conditions. Thus our new spectral measurements demonstrate the high sensitivity of minerals to environmental conditions under which they are measured and provide important constraints for interpreting new thermal infrared data sets of the Moon, including Diviner data.

4.1.1. Plagioclase

[16] Plagioclase feldspar ($[\text{Ca}, \text{Na}]\text{Al}_2\text{Si}_2\text{O}_8$) is one of the most common silicate minerals in the lunar crust. The

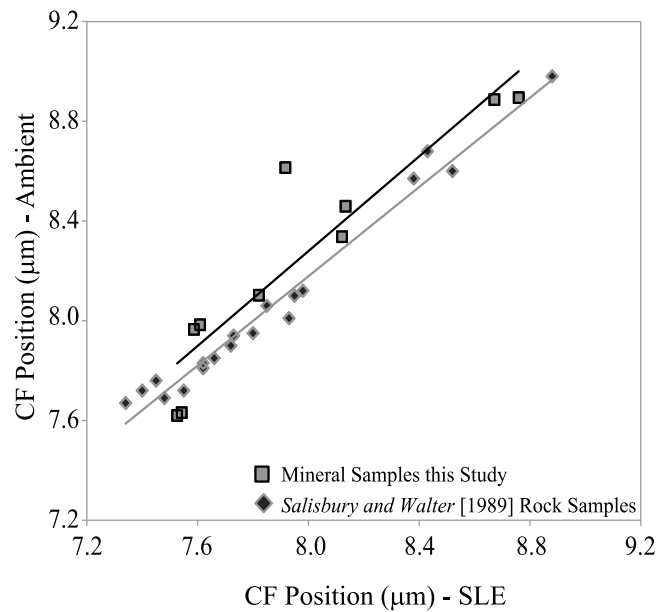


Figure 6. The CF position measured under SLE and ambient conditions for rock and mineral spectra. The black diamond data points are taken from *Salisbury and Walter* [1989] and include a range of rock compositions (felsic to mafic). The gray line is the linear fit to the powdered rock data with the equation: $y = 0.8950x + 1.0181$ and an $R^2 = 0.9773$. The gray square data points are taken from Table 5 and include the silicate minerals. The black line is the linear fit to the powdered mineral data with the equation: $y = 0.9502x + 0.6778$ and an $R^2 = 0.8516$.

majority of plagioclase likely crystallized in the late stages of the lunar magma ocean and formed the lunar crust by floatation to the surface due to the density difference between it and the previously crystallized mafic cumulates [*Warren*, 1985; *Wood*, 1986]. Analyses of Apollo hand samples indicate a small range in An content for the ferroan anorthosites (An_{94-98}) and a larger An content for Mg and Alkali-suite rocks (An_{65-98}) [*Papike*, 1998]. *Nash and Salisbury* [1991] showed that the in laboratory reflectance spectra of fine particulate samples of the plagioclase solid solution series that: (1) the CF position can be used to distinguish between plagioclase compositions and (2) the CF position has a linear relationship with the An content of the plagioclase composition. *Ruff* [1998] measured well-characterized coarse particulate samples of alkali and plagioclase feldspars using thermal infrared emission spectroscopy and identified key differences in the fundamental molecular vibrations to distinguish between feldspar compositions. Recent thermal infrared observations on the Moon

Table 4. Positions of CF, RB, and TF for the Silicate Minerals

Mineral	Ambient Band Position, cm^{-1}										SLE Band Position, cm^{-1}									
	CF	TF	RB1	RB2	RB3	RB4	RB5	RB6	RB7	RB8	CF	TF	RB1	RB2	RB3	RB4	RB5	RB6	RB7	RB8
Albite	1312	853	1189	1091	1037	1004	658	597	531		1329		1188	1094	1037	1006	653	600	534	
Anorthite	1234	836	1146	1025	931	624	584	539	471	416	1279		1125	1027	949	626	585	541	471	424
Enstatite	1200	800	1061	973	957	872	570	540	507	450	1231		1061	972	956	874	568	541	510	448
Augite	1182	740	1117	1009	957	909	542	509	470		1229		1108	1006	960	914	541	516	472	
Forsterite	1124	777	1055	984	943	625	524	471	421		1142	793	1032	983	942	620	525	470	418	

by Diviner: (1) determined anorthite and intermediate plagioclase compositions like bytownite and labradorite for areas previously identified as plagioclase-rich regions [Greenhagen *et al.*, 2010; Ohtake *et al.*, 2009] and (2) identified unique areas on the lunar surface with CF positions at higher wave numbers than Ca-rich plagioclase, anorthite, indicating areas comprised of quartz and/or Na- and K-rich feldspar [Glotch *et al.*, 2010; Greenhagen *et al.*, 2010].

[17] Here we focus on two end-members from the plagioclase solid solution series: albite (An_{01}) and anorthite (An_{90}) seen in Figure 3. Table 4 lists the positions in wave numbers (cm^{-1}) of the CF, TF and RB absorptions identified in Figure 3 for ambient and SLE conditions. At a spectral sampling of 2 cm^{-1} , the theoretical error in band minimum identification is $\pm 2 \text{ cm}^{-1}$, although that error likely increases for broad absorption features. The fundamental absorptions of the RB are sharper in the albite spectra versus the anorthite spectra under both conditions as previously observed by Ruff [1998] under ambient conditions for coarse plagioclase samples. Under SLE conditions, the first RB absorption (RB1 identified in Figure 3) in the albite and anorthite spectra broadens, this causes the band minima to shift to lower wave numbers compared to band minima identified in the ambient spectra. All other differences in positions of identified RB band minima are within the spectral sampling error of $\pm 2 \text{ cm}^{-1}$.

[18] In alkali feldspars like albite, a strong absorption centered at 600 cm^{-1} is bounded by two weaker absorptions, producing a triple absorption arrangement that is unique among the silicates [Ruff, 1998]. Plagioclase feldspars (anorthite) have many of the same absorptions, but in most cases they are shallower and/or broader than those of the alkali feldspars. In our ambient albite spectrum, a strong absorption centered at 597 cm^{-1} (RB6) is bounded by weaker absorptions at 658 cm^{-1} (RB5) and 531 cm^{-1} (RB7). Under SLE conditions, the triple absorptions occur at similar positions, however the RB5 and RB7 absorptions have greater depth and width than the ambient absorptions. In our ambient anorthite spectrum, the triple absorption features (identified as RB4, RB5, and RB6 in Figure 3) are weaker than the albite triple absorption features, both in SLE and ambient conditions. The triple absorption band positions occur at similar positions under ambient and SLE conditions for albite and anorthite.

4.1.2. Pyroxene

[19] Orthopyroxene ($[\text{Mg,Fe}]_2\text{Si}_2\text{O}_6$) and clinopyroxene ($[\text{CaMgFe}]_2\text{Si}_2\text{O}_6$) are abundant on the lunar surface in mare basalts, exposures of the lower crust or in exposed plutons [Jolliff *et al.*, 2006]. Lunar pyroxenes are primarily quadrilateral in their compositions as defined within the compositional space bounded by enstatite-ferrosilite-diopside-hedenbergite and the most common varieties are hypersthene, augite, and pigeonite [Papike, 1998]. Hamilton [2000] identified and characterized the critical spectral absorptions in thermal infrared emissivity spectra of pyroxenes determining the shift in wavelength position, variance in number, and the change in shape as a function of pyroxene silicate structure and cation substitution. Thus a pyroxenes unique composition can be determined using the spectral absorptions in a thermal infrared emissivity spectrum.

[20] Here we focus on a single composition of clinopyroxene and orthopyroxene: enstatite and augite. Eight RB absorptions are identified in the enstatite spectra in Figure 4

and their band positions are listed in Table 4. While the band positions and shapes of these absorptions do not shift under SLE conditions, the spectral contrasts of these absorptions do decrease. In Figure 4, seven RB absorptions are identified for augite. Under SLE conditions, the first RB absorption (RB1) broadens causing the band minimum to shift to lower wave numbers compared to the band minimum identified in the ambient spectrum. The band positions of the remaining RB absorptions do not change under SLE conditions, but their spectral contrast does.

4.1.3. Olivine

[21] Olivine ($[\text{MgFe}]_2\text{SiO}_4$) is a major component of the lunar mantle and is observed on the lunar surface in varying abundances in mare basalts as well as in the central peaks of craters [e.g., Pieters, 1982; Lucey *et al.*, 1986; Tompkins and Pieters, 1999] and around lunar impact basins [Yamamoto *et al.*, 2010]. Most olivines in mare basalts have compositions ranging from Fo_{80-90} although there are a few mare basalts that have olivines with compositions ranging from Fo_{0-10} [Jolliff *et al.*, 2006]. The composition of the olivine (high Fo value versus low Fo value) indicates the primitive or evolved nature of the source from which the olivines crystallized [Basaltic Volcanism Study Project, 1981]. Also lunar olivines are often chromite-bearing making their VNIR spectra different from their terrestrial olivine counterparts giving rise to adverse effects on modeling the compositions of remotely sensed olivine in the NIR [Isaacson and Pieters, 2010].

[22] Here we focus on a single end-member of olivine: forsterite. Seven RB absorptions are identified, in ambient and SLE spectra in Figure 5 and their band positions are listed in Table 4. The first RB absorption (RB1) is broader in the SLE spectrum, thus shifting the band minimum to a lower wave number position. The other RB absorptions do not change in position under SLE conditions, but they do decrease in spectral contrast; however the decrease in spectral contrast in forsterite is less than the spectral contrast decrease in albite, anorthite, enstatite, and augite. A TF centered at 777 cm^{-1} is identified in the ambient spectrum, but the TF is shifted to a higher wave number position (793 cm^{-1}) in the SLE spectrum. Forsterite's TF in SLE conditions is the most apparent of all mineral TF in the $768\text{--}908 \text{ cm}^{-1}$ spectral range.

4.2. Spectral Parameter Results: Lab Applications to Diviner Data

[23] The Diviner Lunar Radiometer Experiment was launched onboard NASA's LRO on June 18, 2009 and has begun making the first global maps of thermal infrared derived compositions [Greenhagen *et al.*, 2010] and thermophysical properties [Paige *et al.*, 2010a, 2010b; Bandfield *et al.*, 2011]. Diviner has three $8 \mu\text{m}$ region channels centered at 7.81 , 8.28 , and $8.55 \mu\text{m}$ that were chosen specifically to measure the peak of the CF [Greenhagen, 2009]. These channels have been used to: (1) map highly silicic compositions on the Moon using spectral parameters that describe the spectral shape of measurements returned by Diviner [Glotch *et al.*, 2010], (2) map global lunar surface compositions using the CF position [Greenhagen *et al.*, 2010], and (3) distinguish between mineral groups and lunar surface lithologies using band ratios of laboratory measurements of minerals and Apollo soil samples [Donaldson Hanna *et al.*, 2009]. Here our full resolution laboratory emissivity spectra measured

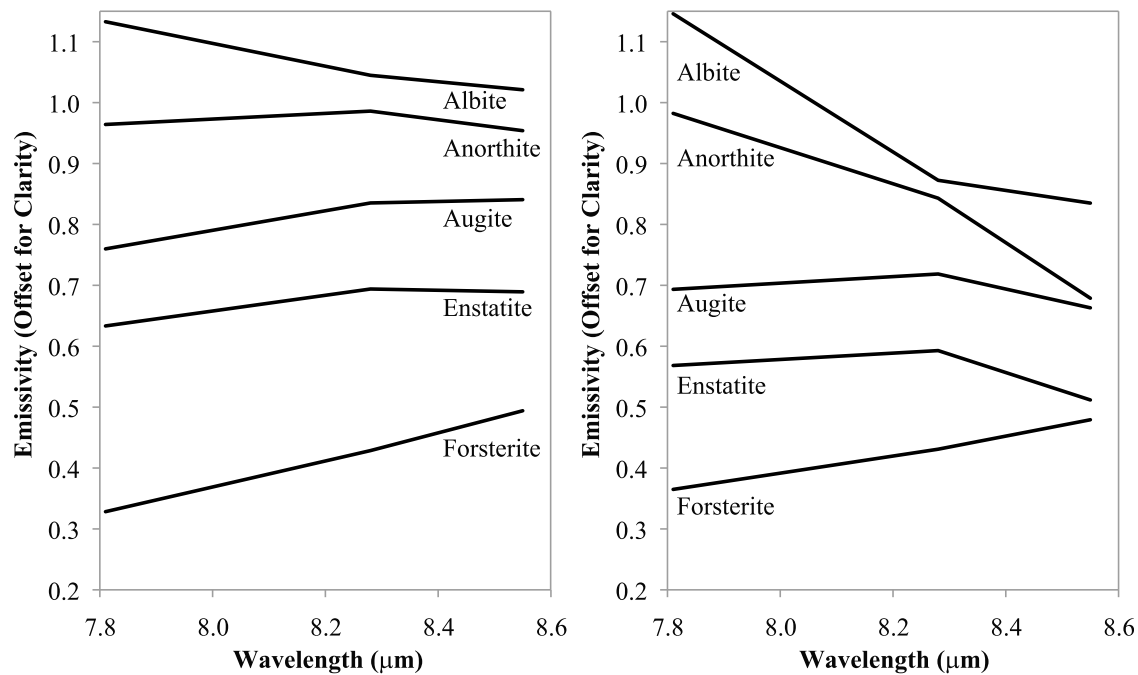


Figure 7. (left) Full resolution laboratory emissivity spectra of the silicate minerals measured under ambient and (right) SLE conditions that have been re-sampled to the three mineralogy channels of Diviner. Spectra are offset by 0.15 emissivity for clarification.

under ambient and SLE conditions are convolved to the three Diviner 8 μm region bands using the Diviner band pass filter functions and plotted in Figure 7 [Paige *et al.*, 2010a]. We discuss the re-sampled laboratory spectra in terms of their spectral shape, CF position, and how band ratios change between ambient and SLE conditions.

4.2.1. Spectral Shape

[24] When analyzing full resolution laboratory spectra of minerals, rocks and soils the overall spectral shape can be identified using distinguishing spectral features. However, when using spectra re-sampled to a small number of bands it is helpful to identify spectral parameters that can highlight differences in spectral shapes. Glotch *et al.* [2010] defined two spectral parameters to distinguish between silicate minerals: I and c . I is defined as the difference between the emissivity at 7.81 μm and at 8.28 μm and is a measure of the slope between

the two points. Spectral parameter c , determines the concavity between the 7.81 μm and 8.55 μm channels. A positive concavity means the spectrum is concave up and a negative concavity means the spectrum is concave down. Spectral parameter values calculated for I and c for our minerals are in Table 5.

[25] Diviner resolution spectra under ambient and SLE conditions are plotted in Figure 5. Albite is the only mineral that has a positive I value and is concave up under ambient and SLE conditions. As the CF shifts to shorter wavelengths under SLE conditions, anorthite is the only mineral that changes behavior. Under ambient conditions anorthite has a concave down shape with a negative I value, while under SLE conditions it is still concave down, but it has a positive I value indicating a change in overall slope. Augite and enstatite are both concave down with negative I values under ambient and SLE conditions while forsterite is concave up

Table 5. Measured and Calculated Spectral Parameters for the Silicate Minerals

Mineral	I	Concavity	Measured CF (μm)	Calculated CF (μm)	Δ CF Position	7.81/8.55	8.55/8.28	7.81/8.28
<i>Ambient</i>								
Albite	0.088	+	7.62	8.74	-1.12	1.13	0.97	1.10
Anorthite	-0.022	-	8.10	8.15	-0.05	1.01	0.97	0.98
Augite	-0.075	-	8.46	8.47	-0.01	0.91	1.03	0.93
Enstatite	-0.061	-	8.34	8.37	-0.03	0.94	1.00	0.94
Forsterite	-0.100	+	8.89	5.30	3.59	0.82	1.07	0.89
<i>SLE</i>								
Albite	0.273	+	7.53	8.53	-1.00	1.55	0.94	1.46
Anorthite	0.139	-	7.82	7.69	0.13	1.45	0.81	1.17
Augite	-0.025	-	8.13	8.12	0.01	1.06	0.97	1.02
Enstatite	-0.024	-	8.12	8.10	0.02	1.06	0.92	0.98
Forsterite	-0.066	+	8.76	6.70	2.16	0.88	1.05	0.93

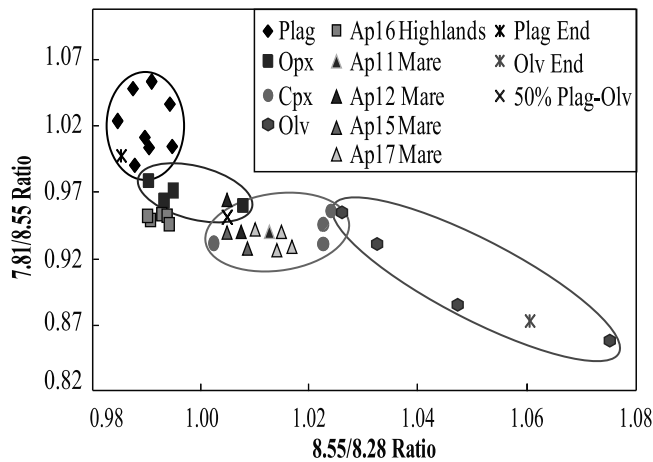


Figure 8. Full resolution laboratory emissivity spectra measured under ambient conditions convolved to the Diviner's three mineralogy channels and then ratioed (7.81/8.55 and 8.55/8.28) for each composition of each mineral group. The different mineral groups are clearly distinguished from one another with plagioclase plotting in the upper left (indicating a shorter CF wavelength) and olivine plotting in the lower right (indicating a longer CF wavelength).

and has a negative I value under ambient and SLE conditions. Our results corroborate findings by *Glotch et al.* [2010] that anorthite and all minerals more silicic than it have positive I values under SLE conditions with albite being the only mineral to also exhibit positive concavity. However, our results show that under ambient conditions only albite has a positive I value. This shows the sensitive nature of the spectral shape to the environment under which it is measured. Also, while the spectral shape parameters I and c are good indicators of minerals and their compositions, they are non-unique and should be used with other spectral parameters for more robust identifications.

4.2.2. CF Position

[26] Diviner's three 8 μm region channels were chosen specifically to measure the CF position across the 7.8–8.6 μm wavelength range [Greenhagen, 2009]. Analysis of fine particulate lunar soil spectra measured under a simulated lunar environment showed that the CF can be fit using a parabola; thus the wavelength position of the CF in Diviner data is estimated by solving three quadratic equations to find the wavelength of the parabola maximum [Greenhagen et al., 2010]. Here the same method of parabolic fitting is applied to our re-sampled laboratory spectra to estimate their CF position. These calculated CF positions are then compared with the CF positions measured in the full resolution laboratory spectra.

[27] In Table 5 the measured CF position from the full resolution laboratory emissivity spectra of minerals, the CF position calculated using a parabolic fit to the re-sampled laboratory emissivity of the same minerals, and the difference between the measured and calculated CF positions are listed for both ambient and SLE conditions. For both ambient and SLE conditions, minerals like anorthite, augite, and enstatite that have measured CF positions in the middle of the Diviner mineralogy channel wavelength range (7.8–8.6 μm) have calculated CF positions to within $\pm 0.03 \mu\text{m}$, equal to the

uncertainty in determining the CF wavelength position from the 2 cm^{-1} resolution laboratory measurements. It is clear that for minerals like albite and forsterite that have measured CF positions outside of the Diviner mineralogy wavelength range the parabolic fitting does a poor job at estimating the CF position and produces results that are inaccurate. It is also worth noting, that as the measured CF position systematically shifts to wavelengths close to the edge of the Diviner wavelength range the difference between the measured and calculated CF position gets larger; this can be seen by looking at the CF position of anorthite under ambient and SLE conditions. As the measured CF position shifts to shorter wavelengths under SLE conditions it also shifts closer to the edge of the Diviner wavelength range and the difference between the measured and calculated CF position gets larger.

[28] Overall the parabolic fitting works well at estimating the wavelength position of the CF for minerals that have CF positions within the Diviner wavelength range. Thus for any rock or soil that has a CF position within this range, its CF position is calculated to a typical accuracy of $\pm 0.03 \mu\text{m}$ at Diviner resolution. The small differences between the measured and calculated CF position for minerals within the Diviner wavelength range could likely result from the assumption of a parabolic fit to the CF. The parabolic assumption is based on lunar samples measured under SLE conditions having a parabolic shape. However, our full resolution laboratory spectra of minerals in Figure 2 shows that under SLE conditions the CF shape deviates from a parabola as the spectral contrast between the CF and RB increases, but the spectral contrast of the TF at wavelengths short of the CF does not increase. For materials with CF positions outside of the Diviner wavelength range, the parabolic fitting does not estimate the CF position well and other approaches (i.e., identifying the concavity of the spectral shape and calculating band ratios) should be used to identify these materials.

4.2.3. Band Ratios

[29] Band ratios are a common and effective way to analyze spectral data sets with a limited number of bands and are optimized to distinguish specific spectral features. As an example, several band ratios have been created to optimize the Clementine UVVIS multispectral data set that has only five spectral channels between 0.4–1.00 μm . Spectral band ratios have been used to determine the composition and distribution of mafic minerals, the approximate abundance of FeO, and the maturity of the surface [e.g., Lucey, 2004; Tompkins and Pieters, 1999; Lucey et al., 1998]. Here we calculate band ratios using Diviner's three 8 μm region channels under ambient and SLE conditions to determine how spectral band ratios can be used to constrain lunar surface compositions.

[30] First, re-sampled ambient spectra of the major mineral groups (plagioclase, low- and high-Ca pyroxene, and olivine) were ratioed to determine which ratios best distinguish the mineral groups from one another. In Figure 8, a combination of the 7.81/8.55 ratio and 8.55/8.28 ratio are plotted for mineral samples of varying composition. The 7.81/8.55 ratio approximates the general trend, concave up or concave down, of the spectrum while the 8.55/8.28 ratio approximates the positive or negative slope between the two spectral channels. The individual minerals groups are clearly distinguished with plagioclase plotting in the upper left

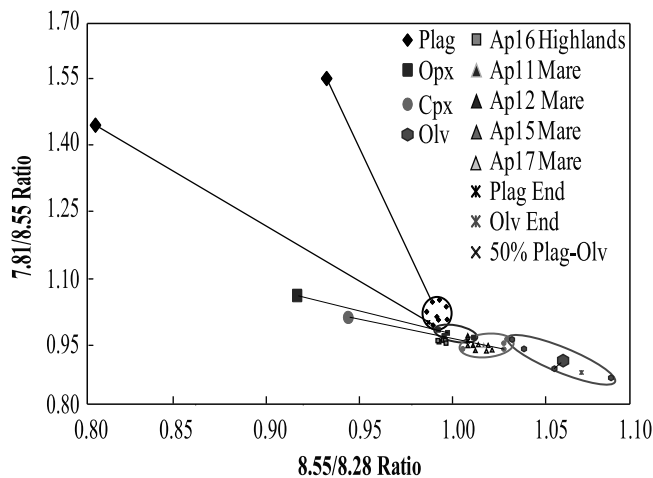


Figure 9. Full resolution laboratory emissivity spectra measured under ambient (small symbols) and SLE (large symbols) conditions convolved to the Diviner's three mineralogy channels and then ratioed (7.81/8.55 and 8.55/8.28) for each composition of each mineral group. Mineral samples that have been measured under both ambient and SLE conditions are connected by black lines.

(CF at shorter wavelengths) and olivine plotting in the lower right (CF at longer wavelengths).

[31] The advantage of using mineral samples measured under ambient conditions is that it allows us to incorporate laboratory reflectance spectra of well-characterized Apollo lunar soil samples [Taylor *et al.*, 2001, 2003] that have not been measured under a simulated lunar environment. The addition of the Apollo lunar soils as well as a 50/50 wt% mineral mixture of anorthite and olivine provides a useful starting point for discussing the soils and mixtures in context of the minerals. In Figure 8, the 7.81/8.55 and 8.55/8.28 ratios are also plotted for the 50/50 wt% mineral mixture of anorthite and olivine, the mixture end-members, and lunar highlands and mare soils. The Apollo 16 highlands soils are clearly distinguished from the Apollo 11, 12, 15 and 17 mare soils. While the highlands soils plot close to the plagioclase mineral group as expected, the mare soils cannot be distinguished from the clinopyroxene group or a mixture of end-members. The anorthite and olivine end-members clearly plot within their appropriate mineral groups, but the 50/50 wt% mineral mixture cannot be distinguished from the clinopyroxene or orthopyroxene groups. While it is possible to distinguish the major lunar lithologies with Diviner thermal infrared band ratios, it is not possible to interpret specific mineral assemblages for them or the simple 50/50 wt% mixture using only three spectral bands.

[32] Figure 9 shows the 7.81/8.55 and 8.55/8.28 band ratios calculated for the re-sampled ambient and SLE mineral spectra where mineral samples measured under both ambient and SLE conditions are connected by lines. Two changes in the mineral spectra due to SLE conditions need to be considered to discuss how the band ratios change between ambient and SLE conditions. First, the shift of the CF position to shorter wavelengths under SLE conditions can change the spectral shape altogether, as shown by anorthite in Figure 7 for example. Next, while the increase in spectral contrast between the CF position and the principal

RB observed under SLE conditions does not change the general shape (concave up or down) or direction of slope (positive or negative) it will change the degree of slope. As the spectral contrast increases the degree of slope also increases affecting both band ratios as seen in Table 5. As seen in Figure 9, all mineral groups are affected in the same way, so while the values on the x- and y-axes change, the trend of distinguishing mineral groups does not. The sensitive nature of the band ratios to the environment under which they are measured illustrate how important it is to replicate the correct lunar environment in the lab when measuring lunar analog materials for comparisons with Diviner and future thermal infrared data sets.

4.3. Thermal and Near Infrared Integration

[33] We now examine the extent to which combined thermal- and near-infrared analyses can be used to constrain the mineralogy of lunar surface lithologies. The CF wavelength position, which has been shown to be a good indicator of composition even under a simulated lunar environment, is integrated with well established near infrared spectral parameters from the Clementine and SELENE and M³ data sets. The integration of data sets across two different wavelength regimes allows us to distinguish between mixtures and lunar lithologies more readily.

4.3.1. Spectral Curvature

[34] Spectral curvature is a near-infrared parameter from the Clementine paradigm that has been used to map small outcrops, craters, and mountains using Clementine multi-spectral data [Tompkins and Pieters, 1999]. Spectral curvature is calculated as the angle between the 0.75, 0.90, and 0.95 μm spectral bands and is used to distinguish between Fe-bearing minerals. The spectral curvature parameter is not intended to be used with mature lunar soils as the 1 μm ferrous band and continuum are strongly coupled and affected by space weathering effects. Since continuum removal is not possible with Clementine data, the Apollo lunar soils, which range from immature ($I_s\text{FeO} < 30$) to mature ($I_s\text{FeO} > 60$) [Taylor *et al.*, 2001, 2003] will not be examined with the spectral curvature parameter.

[35] Spectral curvature values are adapted for each mineral group (plagioclase, low- and high-Ca pyroxene, and olivine) and the 50/50 wt% mineral mixture from Tompkins and Pieters [1999]. The CF wavelength position is the peak position measured under SLE conditions. For laboratory emissivity spectra measured under ambient conditions at PEL, the CF position under SLE conditions are calculated using the measured ambient CF position and the linear relationship in Figure 6. Figure 10 shows spectral curvature plotted against SLE CF wavelength position for each mineral end-member and the 50/50 wt% anorthite and olivine mixture and its end-members. While the CF position clearly distinguishes each mineral group, the addition of spectral curvature separates the 50/50 mixture of plagioclase and olivine from the low- and high-Ca mineral groups. This result suggests that immature lunar surface lithologies with varying abundances of mafic minerals can be separated using an integration of these two diagnostic spectral parameters.

4.3.2. Band Minimum

[36] In the paradigm of hyperspectral data sets like SELENE and M³ a 1 μm band minimum is calculated. Spectral measurements in the visible-to-near infrared wavelengths identify

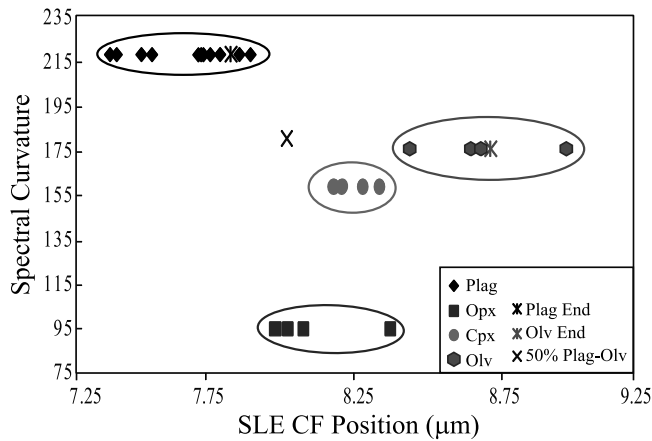


Figure 10. NIR parameter, spectral curvature, plotted against the SLE CF position for individual minerals as well as the 50/50 wt% mixture as determined by *Tompkins and Pieters* [1999]. The width of each ellipse indicates the range in composition for that mineral group. With the addition of spectral curvature, the mineral groups are no longer overlapping and it is clear that the 50/50 wt% mixture is not a low- or high-Ca pyroxene.

Fe-bearing minerals such as pyroxenes, plagioclase and olivine by using broad absorptions at characteristic wavelengths caused by electronic transitions of Fe^{2+} . In particular, the wavelength position of the $1\ \mu\text{m}$ band minimum can be used to distinguish between Fe-bearing minerals. Pyroxenes have a diagnostic absorption band around $1\ \mu\text{m}$, with the position of the band changing as composition changes [e.g., *Adams*, 1974; *Hazen et al.*, 1978; *Cloutis et al.*, 1986; *Klima et al.*, 2007]. The identification of Fe-bearing crystalline plagioclase in the NIR is based on a broad absorption band at approximately $1.3\ \mu\text{m}$ due to trace amounts of Fe^{2+} being incorporated into the crystal structure. Laboratory studies of plagioclase has shown that the band depth and center position of the diagnostic $1.3\ \mu\text{m}$ band may vary with Fe abundance and An# respectively [Adams and McCord, 1971; Bell and Mao, 1973; Adams and Goullaud, 1978; Cheek et al., 2009]. Olivine has three overlapping absorptions between $0.9\text{--}1.25\ \mu\text{m}$ and these absorptions shift to longer wavelengths as the Fe content increases [e.g., *Burns*, 1970; *Sunshine and Pieters*, 1998].

[37] Since the spectral range of measurements made in Berlin and Oxford is restricted to the TIR, RELAB NIR laboratory reflectance spectra of a range of compositions for each mineral group (plagioclase, clinopyroxene, orthopyroxene, and olivine) as well as laboratory near infrared reflectance spectra of the Apollo lunar soils are used. The band minimum for each mineral and lunar soil spectrum is calculated by finding the minimum value between $0.8\text{--}1.30\ \mu\text{m}$ for a continuum-removed spectrum. In Figure 11, band minimum is plotted against the SLE CF wavelength position for each mineral group and lunar soil. Again, for laboratory emissivity and reflectance spectra measured under ambient conditions at PEL and RELAB, the CF position under SLE conditions are calculated using the measured ambient CF position and the linear relationship in Figure 6. The boxes represent the range of compositions for each individual mineral group. The width of each box represents the range in compositions for the thermal infrared measured

minerals and the height represents the range in compositions of near infrared measured minerals measured at near infrared wavelengths. Mineral groups and lunar lithologies are clearly separated from one another. Both the lunar highlands and mare soils plot near the low- and high-Ca pyroxene groups. While the anorthositic highlands are predominantly composed of plagioclase they do contain some pyroxene. It is likely that the pyroxene band minimum is dominating the spectra making the highlands soils plot along with the pyroxene groups. Clearly, using the strengths of the near infrared and integrating those with the strengths of the thermal infrared will enable more robust determinations of surface compositions using current and future data sets.

5. Future Work

[38] Here we began with the characterization of pure minerals, as they are the easiest to characterize under varying environmental conditions, however it is understood that most of the lunar surface is covered in regolith that is a complex mixture of minerals, glasses, and agglutinates. Future spectral measurements will focus on building a spectral library of well-characterized Apollo lunar soils and rocks as well as lunar meteorites as they are the most applicable to TIR data currently being collected by Diviner as well as any future hyperspectral TIR data sets. In the tradition of other spectral databases [Christensen et al., 2000; Pieters and Hiroi, 2004; Clark et al., 2007; Maturilli et al., 2008], we will also measure various compositions of minerals known to be on the lunar surface for use as spectral end-members as well as for mixture analysis. Having a large spectral library of lunar analog materials

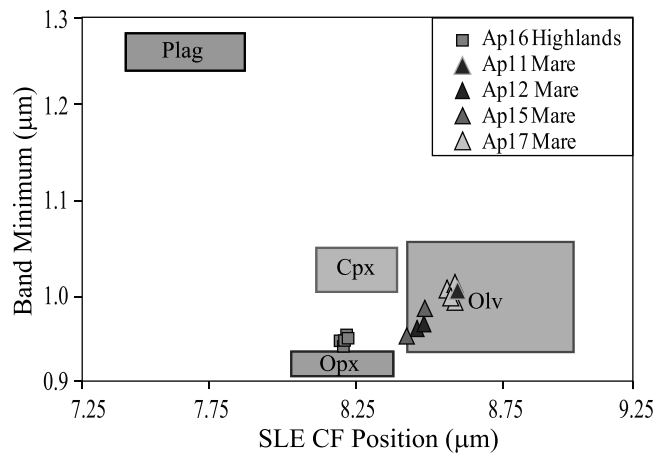


Figure 11. NIR parameter, $1\ \mu\text{m}$ band minimum plotted against the SLE CF wavelength position for individual minerals and Apollo lunar soils. Apollo lunar soils were measured at NIR and TIR wavelengths in RELAB. The width of each box represents the range of compositions for each mineral group as measured at thermal infrared wavelengths and the height of each box represents the range of compositions for minerals measured at near infrared wavelengths. With the addition of band minimum, mineral groups and lunar lithologies are easily separated. Unlike integrated band depth, the range of band minima values for the lunar soils is only an indication of the composition of the mafic minerals.

measured under a simulated lunar environment will allow us to better understand how to distinguish lunar lithologies using Diviner data.

6. Conclusions

[39] (1) This is the first characterization of laboratory emissivity measurements of minerals across the $400 \sim 1700 \text{ cm}^{-1}$ ($6\text{--}25 \mu\text{m}$) spectral range measured under a simulated lunar environment. All previous lab studies focused on the $909\text{--}1428 \text{ cm}^{-1}$ ($7\text{--}11 \mu\text{m}$) spectral range. The added spectral range from $400\text{--}833 \text{ cm}^{-1}$ ($12\text{--}25 \mu\text{m}$) encompasses RB absorptions that are as indicative of mineral composition as the RB absorptions between $833\text{--}1250 \text{ cm}^{-1}$ ($8\text{--}12 \mu\text{m}$).

[40] (2) Laboratory TIR emissivity spectra of the major silicate minerals on the Moon made under SLE conditions show several differences from those measured under ambient conditions: (a) the CF position shifts to higher wave numbers (shorter wavelengths), (b) the overall spectral contrast increases, (c) the spectral contrast of the RB and TF decrease, and (d) the spectral contrast of RB absorptions between $400\text{--}625 \text{ cm}^{-1}$ (16 and $25 \mu\text{m}$) also decrease. The shift in the CF position corroborates previous lab studies by Logan et al. [1973] and our linear trend between the ambient CF position and the SLE CF position corroborates work by Salisbury and Walter [1989]. Both lab studies [Logan et al., 1973; Salisbury and Walter, 1989] focused on laboratory reflectance spectra of powered rock samples of varying compositions while ours focused on laboratory emissivity spectra of powdered mineral samples.

[41] (3) Diviner's three mineralogical spectral channels allow us to: (a) use spectral parameters to distinguish some minerals from one another by looking at their spectral slopes and concavities, (b) approximate the CF position to within $\pm 0.03 \mu\text{m}$ for rocks, minerals and soils that have CF positions within the Diviner mineralogical wavelength range, (c) use thermal infrared band ratios to distinguish between individual mineral groups as well as distinguish between plagioclase compositions, (d) distinguish between lunar lithologies (i.e., mare basalt versus anorthositic highlands), and (e) integrate TIR and NIR data sets to permit unique identification of both individual mineral groups and lunar surface lithologies given the geologic context of a measured region.

[42] (4) While TIR Diviner data can be used to constrain mineral type, mineral compositions, and lunar lithologies, the limited number of spectral bands and fine particulate nature of the lunar surface make it difficult to uniquely separate simple and complex mixtures. Integrating Diviner TIR data with current and future VNIR spectral measurements will allow us to make more robust compositional identifications on the lunar surface. The integration of a TIR spectral band ratio with the $1 \mu\text{m}$ band minimum allowed us to unambiguously identify mineral groups from one another. Spectral measurements of mineral mixtures over the complete VNIR to TIR wavelength region will allow us to better understand how the integration of data sets from two different wavelength ranges can best be utilized for the Diviner and other future data sets.

[43] **Acknowledgments.** We would like to extend our appreciation to P. Christensen and Arizona State University for donating the samples used in this study. The authors would also like to thank S. Ruff and an anonymous reviewer for comments and suggestions that have helped to improve the

manuscript as well as C. M. Pieters for comments and suggestions that greatly improved the thermal- and near-infrared data integration portion of this manuscript. K. L. Donaldson Hanna and M. B. Wyatt were supported by NASA grant NNX08AM75G.

References

- Adams, J. B. (1974), Visible and near-infrared diffuse reflectance spectra of pyroxenes as applied to remote sensing of solid objects in the solar system, *J. Geophys. Res.*, **79**, 4829–4836, doi:10.1029/JB079i032p04829.
- Adams, J. B., and L. H. Goulaud (1978), Plagioclase feldspars: Visible and near infrared diffuse reflectance spectra as applied to remote sensing, *Proc. Lunar Planet. Sci. Conf.*, **9th**, 2901.
- Adams, J. B., and T. B. McCord (1971), Optical properties of mineral separates, glass, and anorthositic fragments from Apollo mare samples, *Proc. Lunar Sci. Conf.*, **2nd**, 2183.
- Bandfield, J. L., R. Ghent, A. Vasavada, D. Paige, S. J. Lawrence, and M. Robinson (2011), Lunar surface rock abundance and regolith fines temperatures derived from LRO Diviner Radiometer data, *J. Geophys. Res.*, **116**, E00H02, doi:10.1029/2011JE003866.
- Basaltic Volcanism Study Project (1981), *Basaltic Volcanism on the Terrestrial Planets*, Pergamon Press, New York.
- Bell, P. M., and H. K. Mao (1973), Optical and chemical analyses of iron in Luna 20 plagioclase, *Geochim. Cosmochim. Acta*, **37**, 755–759, doi:10.1016/0016-7037(73)90172-5.
- Burns, R. G. (1970), *Mineralogical Applications of Crystal-Field Theory*, Cambridge Univ. Press, London.
- Cheek, L. C., C. M. Pieters, M. D. Dyar, and K. A. Milam (2009), Revisiting plagioclase optical properties for lunar exploration, *Proc. Lunar Planet. Sci. Conf.*, **40th**, 1928.
- Christensen, P. R., J. L. Bandfield, V. E. Hamilton, D. A. Howard, M. D. Lane, J. L. Piatek, S. W. Ruff, and W. L. Stefanov (2000), A thermal emission spectral library of rock-forming minerals, *J. Geophys. Res.*, **105**, 9735–9739, doi:10.1029/1998JE000624.
- Christensen, P. R., et al. (2001), Mars Global Surveyor Thermal Emission Spectrometer experiment: Investigation description and surface science results, *J. Geophys. Res.*, **106**, 23,823–23,871, doi:10.1029/2000JE001370.
- Christensen, P. R., B. M. Jakosky, H. H. Kieffer, M. C. Malin, H. Y. McSweeney, K. Nealson, G. L. Mehall, S. H. Silverman, S. Ferry, and M. Caplinger (2004), The Thermal Emission Imaging System (THEMIS) for the Mars 2001 Odyssey Mission, *Space Sci. Rev.*, **110**, 85–130, doi:10.1023/B:SPAC.0000021008.16305.94.
- Clark, R. N., G. A. Swayze, R. Wise, E. Livo, T. Hoefen, R. Kokaly, and S. J. Sutley (2007), USGS digital spectral library splib06a, *Digital Data Ser. 231*, U.S. Geol. Surv., Denver, Colo.
- Cloutis, E. A., M. J. Gaffey, T. L. Jackowski, and K. L. Reed (1986), Calibrations of phase abundance, composition, and particle size distribution for olivine-orthopyroxene mixtures from reflectance spectra, *J. Geophys. Res.*, **91**, 11,641–11,653, doi:10.1029/JB091iB11p11641.
- Conel, J. E. (1969), Infrared emissivities of silicates: Experimental results and a cloudy atmospheric model of spectral emission from condensed particulate mediums, *J. Geophys. Res.*, **74**, 1614–1634, doi:10.1029/JB074i006p01614.
- Cooper, B. L., J. W. Salisbury, R. M. Killen, and A. E. Potter (2002), Mid infrared spectra features and their powders, *J. Geophys. Res.*, **107**(E4), 5017, doi:10.1029/2000JE001462.
- Donaldson Hanna, K. L., M. B. Wyatt, J. Helbert, A. Maturilli, and C. M. Pieters (2009), Constraining lunar surface mineralogy with combined thermal- and near-infrared spectral data, *Proc. Lunar Planet. Sci. Conf.*, **40th**, 2286.
- Fischer, E. M. (1995), Quantitative compositional analysis of the lunar surface from reflectance spectroscopy: Iron, aluminum, and a model for removing the optical effects of space weathering, Ph.D. diss., Brown Univ., Providence, R. I.
- Glotch, T. D., et al. (2010), Highly silicic compositions on the Moon, *Science*, **329**, 1510–1513, doi:10.1126/science.1192148.
- Goetz, A. F. H. (1968), Differential infrared lunar emission spectroscopy, *J. Geophys. Res.*, **73**, 1455–1466, doi:10.1029/JB073i004p01455.
- Greenhagen, B. T. (2009), Thermal emission remote sensing of the Moon: Design and development of Diviner Lunar Radiometer compositional capabilities, Ph.D. diss., Univ. of Calif., Los Angeles.
- Greenhagen, B. T., et al. (2010), Global silicate mineralogy of the Moon from the Diviner Lunar Radiometer, *Science*, **329**, 1507–1509, doi:10.1126/science.1192196.
- Hamilton, V. E. (2000), Thermal infrared emission spectroscopy of the pyroxene mineral series, *J. Geophys. Res.*, **105**, 9701–9716, doi:10.1029/1999JE001112.
- Hapke, B. (1996), Applications of an energy transfer model to three problems in planetary regoliths: The solid-state greenhouse, thermal beaming, and

- emittance spectra, *J. Geophys. Res.*, **101**, 16,833–16,840, doi:10.1029/96JE00918.
- Hazen, R. M., P. M. Bell, and H. K. Mao (1978), Effects of compositional variation on absorption spectra of lunar pyroxenes, *Proc. Lunar Planet. Sci. Conf.*, **9th**, 2919.
- Hunt, G. R., and J. W. Salisbury (1964), Lunar surface features: Mid-infrared spectral observations, *Science*, **146**, 641–642, doi:10.1126/science.146.3644.641.
- Hunt, G. R., and J. W. Salisbury (1969), A discussion on infrared astronomy, *Philos. Trans. R. Soc. London, Ser. A*, **264**(1150), 109–139.
- Isaacson, P. J., and C. M. Pieters (2010), Deconvolution of lunar olivine reflectance spectra: Implications for remote compositional assessment, *Icarus*, **210**, 8–13, doi:10.1016/j.icarus.2010.06.004.
- Isaacson, P. J., Y. Liu, A. Patchen, C. M. Pieters, and L. A. Taylor (2009), Integrated analyses of lunar meteorites: Expanded data for lunar ground truth, *Proc. Lunar Planet. Sci. Conf.*, **40th**, 2119.
- Isaacson, P. J., Y. Liu, A. D. Patchen, C. M. Pieters, and L. A. Taylor (2010), Spectroscopy of lunar meteorites as constraints for ground truth: Expanded sample collection diversity, *Proc. Lunar Planet. Sci. Conf.*, **41st**, 1553.
- Isaacson, P. J., A. Basu Sarbadhikari, C. M. Pieters, R. L. Klima, T. Hiroi, Y. Liu, and L. A. Taylor (2011), The lunar rock and mineral characterization consortium: Deconstruction and integrated mineralogical, petrological, and spectroscopic analyses of mare basalts, *Meteorit. Planet. Sci.*, **46**, 228–251, doi:10.1111/j.1945-5100.2010.01148.x.
- Jolliffe, B. L., M. A. Wiczorek, C. K. Shearer, and C. R. Neal (Eds.) (2006), *New Views of the Moon*, *Rev. Mineral. Geochem.*, vol. 60, Mineral. Soc. Am., Washington, D. C.
- Klima, R. L., C. M. Pieters, and M. D. Dyar (2007), Spectroscopy of synthetic Mg-Fe pyroxenes: I. Spin-allowed and spin-forbidden crystal field bands in the visible and near-infrared, *Meteorit. Planet. Sci.*, **42**, 235–253, doi:10.1111/j.1945-5100.2007.tb00230.x.
- Logan, L. M., and G. R. Hunt (1970), Emission spectra of particulate silicates under simulated lunar conditions, *J. Geophys. Res.*, **75**(32), 6539–6548, doi:10.1029/JB075i032p06539.
- Logan, L. M., G. R. Hunt, J. W. Salisbury, and S. R. Balsamo (1973), Compositional implications of Christiansen frequency maximums for infrared remote sensing applications, *J. Geophys. Res.*, **78**, 4983–5003, doi:10.1029/JB078i023p04983.
- Lucey, P. G. (2004), Mineral maps of the Moon, *Geophys. Res. Lett.*, **31**, L08701, doi:10.1029/2003GL019406.
- Lucey, P. G., B. R. Hawke, T. B. McCord, C. M. Pieters, and J. W. Head (1986), A compositional study of the Aristarchus region of the Moon using near-infrared reflectance spectroscopy, *J. Geophys. Res.*, **91**, D344–D354, doi:10.1029/JB091iB04p0D344.
- Lucey, P. G., D. T. Blewett, and B. R. Hawke (1998), Mapping the FeO and TiO₂ content of the lunar surface with multispectral imagery, *J. Geophys. Res.*, **103**, 3679–3699, doi:10.1029/97JE03019.
- Lyon, R. J. P. (1964), Evaluation of infrared spectrophotometry for compositional analysis of lunar and planetary soils, part II, Rough and powdered surfaces, *NASA Rep. CR-100*, 264 pp.
- Matsunaga, T., et al. (2008), Discoveries on the lithology of lunar crater central peaks by SELENE Spectral Profiler, *Geophys. Res. Lett.*, **35**, L23201, doi:10.1029/2008GL035868.
- Maturilli, A., J. Helbert, and L. Moroz (2008), The Berlin emissivity database (BED), *Planet. Space Sci.*, **56**, 420–425, doi:10.1016/j.pss.2007.11.015.
- McCleese, D. J., J. T. Schofield, F. W. Taylor, S. B. Calcutt, M. C. Foote, D. M. Kass, C. B. Leovy, D. A. Paige, P. L. Read, and R. W. Zurek (2007), Mars Climate Sounder: An investigation of thermal and water vapor structure, dust and condensate distributions in the atmosphere, and energy, balance of the polar regions, *J. Geophys. Res.*, **112**, E05S06, doi:10.1029/2006JE002790.
- McCord, T. B., R. N. Clark, B. R. Hawke, L. A. McFadden, P. D. Owensby, C. M. Pieters, and J. B. Adams (1981), Moon: Near-infrared spectral reflectance, a good first look, *J. Geophys. Res.*, **86**, 10,883–10,892, doi:10.1029/JB086iB11p10883.
- Murcray, F. H. (1965), The spectral dependence of lunar emissivity, *J. Geophys. Res.*, **70**, 4959–4962, doi:10.1029/JZ070i019p04959.
- Murcray, F. H., D. G. Murcray, and W. J. Williams (1970), Infrared emissivity of lunar surface features 1. Balloon-borne observations, *J. Geophys. Res.*, **75**, 2662–2669, doi:10.1029/JB075i014p02662.
- Mustard, J. F., C. M. Pieters, P. J. Isaacson, J. W. Head, R. L. Klima, N. E. Petro, M. Staid, J. M. Sunshine, C. Runyon, and L. A. Taylor (2010), Compositional characteristics of the Aristarchus crater from (M³) data, *Proc. Lunar Planet. Sci. Conf.*, **41st**, 2000.
- Nash, D. B., and J. W. Salisbury (1991), Infrared reflectance spectra (2.2–15 μ m) of plagioclase feldspars, *Geophys. Res. Lett.*, **18**, 1151–1154, doi:10.1029/91GL01008.
- Ohtake, M., et al. (2009), The global distribution of pure anorthosite on the Moon, *Nature*, **461**, 236–241, doi:10.1038/nature08317.
- Paige, D. A., et al. (2010a), The Lunar Reconnaissance Orbiter Diviner Lunar Radiometer Experiment, *Space Sci. Rev.*, **150**, 125–160, doi:10.1007/s11214-009-9529-2.
- Paige, D. A., et al. (2010b), Diviner Lunar Radiometer observations of cold traps in the Moon's south polar region, *Science*, **330**, 479–482, doi:10.1126/science.1187726.
- Papike, J. J. (Ed.) (1998), *Planetary Materials, Rev. Mineral.*, vol. 36, 864 pp., Mineral. Soc. Am., Washington, D. C.
- Pieters, C. M. (1982), Copernicus crater central peak: Lunar mountain of unique composition, *Science*, **215**, 59–61, doi:10.1126/science.215.4528.59.
- Pieters, C. M. (1993), Compositional diversity and stratigraphy of the lunar crust derived from reflectance spectroscopy, in *Remote Geochemical Analyses: Elemental and Mineralogical Composition*, edited by C. M. Pieters and P. Englert, pp. 309–336, Cambridge Univ. Press, Houston, Tex.
- Pieters, C., and T. Hiroi (2004), RELAB (Reflectance experiment laboratory): A NASA multispectral spectroscopy facility, *Proc. Lunar Planet. Sci. Conf.*, **35th**, 1720.
- Pieters, C. M., E. M. Fischer, O. Rode, and A. Basu (1993), Optical effects of space weathering: The role of the finest fraction, *J. Geophys. Res.*, **98**, 20,817–20,824, doi:10.1029/93JE02467.
- Pieters, C. M., et al. (2009), Mineralogy of the lunar crust in spatial context: First results from the Moon Mineralogy Mapper (M3), *Proc. Lunar Planet. Sci. Conf.*, **40th**, 2052.
- Ruff, S. W. (1998), Quantitative thermal infrared emission spectroscopy applied to granulite petrology, Ph. D. diss., Ariz. State Univ., Tempe, Ariz.
- Salisbury, J. W., and L. S. Walter (1989), Thermal infrared (2.5–13.5 microns) spectroscopic remote sensing of igneous rock types on particulate planetary surfaces, *J. Geophys. Res.*, **94**, 9192–9202, doi:10.1029/JB094iB07p09192.
- Sprague, A. L., F. C. Witteborn, R. W. Kozlowski, D. P. Cruikshank, M. J. Bartholomew, and A. L. Graps (1992), The Moon: Mid-infrared (7.5- to 11.4 mm) spectroscopy of selected regions, *Icarus*, **100**, 73–84, doi:10.1016/0019-1035(92)90019-4.
- Stoefler, D., H. D. Knoell, U. B. Marvin, C. H. Simonds, and P. H. Warren (1980), Recommended classification and nomenclature of lunar highland rocks: A committee report, in *Proceedings of the Conference on the Lunar Highlands Crust*, Houston, Texas, November 14–16, 1979, A81-26201 10-91, pp. 51–70, Pergamon Press, New York.
- Sunshine, J. M., and C. M. Pieters (1998), Determining the composition of olivine from reflectance spectroscopy, *J. Geophys. Res.*, **103**, 13,675–13,688, doi:10.1029/98JE01217.
- Taylor, L. A., C. Pieters, L. P. Keller, R. V. Morris, D. S. McKay, A. Patchen, and A. Wentworth (2001), The effects of space weathering on Apollo 17 mare soils: Petrographic and chemical characterization, *Meteorit. Planet. Sci.*, **36**, 285–299, doi:10.1111/j.1945-5100.2001.tb01871.x.
- Taylor, L. A., C. Pieters, A. Patchen, D. H. Taylor, R. V. Morris, L. P. Keller, and D. S. McKay (2003), Mineralogical characterization of lunar highland soils, *Proc. Lunar Planet. Sci. Conf.*, **34th**, 1774.
- Thomas, I. R., N. E. Bowles, B. T. Greenhagen, T. D. Glotch, K. L. Donaldson Hanna, M. B. Wyatt, J. L. Bandfield, and D. A. Paige (2010), Emission measurements of lunar analogues for interpretation of returning data from the Diviner Lunar Radiometer on NASA's Lunar Reconnaissance Orbiter, *Proc. Lunar Planet. Sci. Conf.*, **41st**, 1364.
- Tompkins, S., and C. M. Pieters (1999), Mineralogy of the lunar crust: Results from Clementine, *Meteorit. Planet. Sci.*, **34**, 25–41.
- Warren, P. H. (1985), The magma ocean concept and lunar evolution, *Annu. Rev. Earth Planet. Sci.*, **13**, 201–240, doi:10.1146/annurev.ea.13.050185.001221.
- Wood, J. A. (1986), Moon over Mauna Loa: A review of the hypothesis of the formation of the Earth's Moon, in *Origin of the Moon*, edited by W. K. Hartmann, R. J. Phillips, and G. J. Taylor, pp. 17–56, Lunar and Planet. Inst., Houston, Tex.
- Yamaguchi, Y., A. B. Kahle, H. Tsu, T. Kawakami, and M. Pinel (1998), Overview of Advanced Spaceborne Thermal Emission and Reflection Radiometer (ASTER), *IEEE Trans. Geosci. Remote Sens.*, **36**, 1062–1071, doi:10.1109/36.700991.
- Yamamoto, S., et al. (2010), Possible mantle origin of olivine around lunar impact basins detected by SELENE, *Nat. Geosci.*, **3**, 533–536, doi:10.1038/ngeo897.

N. E. Bowles and I. R. Thomas, Atmospheric, Oceanic and Planetary Physics, Clarendon Laboratory, University of Oxford, Parks Road, Oxford OX1 3PU, UK.

K. L. Donaldson Hanna and M. B. Wyatt, Department of Geological Sciences, Brown University, Box 1846, Providence, RI 02912, USA. (kerri_donaldson_hanna@brown.edu)

B. T. Greenhagen, Geophysics and Planetary Geosciences Group, Jet Propulsion Laboratory, M/S 183-301, 4800 Oak Grove Dr., Pasadena, CA 91109, USA.

J. Helbert and A. Maturilli, German Aerospace Center, Institute of Planetary Research, Experimental Planetary Physics, Rutherfordstrasse 2, 12489 Berlin, Germany.

D. A. Paige, Department of Earth and Space Sciences, University of California, Los Angeles, 595 Charles Young Drive East, Box 951567, Los Angeles, CA 90095-1567, USA.